remote sensing

MDPI

Article

Statistical Evaluation of the Performance of Gridded Daily Precipitation Products from Reanalysis Data, Satellite Estimates, and Merged Analyses over Global Land

Weihua Cao [1], Suping Nie [2,3,4,*], Lijuan Ma [5] and Liang Zhao [6]

[1] Institute of Urban Meteorology, China Meteorological Administration, Beijing 100089, China; whcao@ium.cn
[2] Earth System Modeling and Prediction Centre, China Meteorological Administration, Beijing 100081, China
[3] Key Laboratory of Earth System Modeling and Prediction, China Meteorological Administration, Beijing 100081, China
[4] State Key Laboratory of Severe Weather, Beijing 100081, China
[5] National Climate Center, China Meteorological Administration, Beijing 100081, China; malj@cma.gov.cn
[6] Institute of Atmospheric Physics, Chinese Academy of Sciences, Beijing 100029, China; zhaol@lasg.iap.ac.cn
* Correspondence: niesp@cma.gov.cn

Abstract: The Beijing Climate Center of the China Meteorological Administration (BCC/CMA) has developed a gauge-satellite-model merged gridded daily precipitation dataset with complete global coverage, called BCC Merged Estimation of Precipitation (BMEP). Using the unified rain gauge dataset from the CPC (CPC-U) as the independent benchmark, BMEP and the four most widely used global daily precipitation products, including the Global Precipitation Climatology Project one-degree daily (GPCP-1DD), the NCEP Climate Forecast System Reanalysis (CFSR), the Interim ECMWF Reanalysis (ERA-interim), and the 55 year Japanese Reanalysis Project (JRA-55), are evaluated over the global land area from January 2003 to December 2016. The results show that all gridded datasets capture the overall spatiotemporal variation of global daily precipitation. All gridded datasets can basically capture the overall spatiotemporal variation of global daily precipitation. However, CFSR data tend to overestimate precipitation intensity and exhibit a spurious positive trend after 2010, attributed to the transition from CFSR to NCEP's Climate Forecast System Version 2 (CFSv2). On the other hand, JRA-55 and ERA-interim data demonstrate higher skill in characterizing spatial and temporal variations, bias, correlation, and RMSE. GPCP-1DD data perform well in terms of bias but show limitations in detecting the interannual variability and RMSE of daily precipitation. Among these evaluated products, BMEP data exhibit the best agreement with CPC-U data in terms of the spatiotemporal variation, pattern, magnitude of variability, and occurrence of rainfall events across different thresholds. These findings indicate that BMEP gridded precipitation data effectively capture the actual characteristics of daily precipitation over global land areas.

Keywords: gridded daily precipitation; merged and reanalysis datasets; global land area; statistical evaluation

Citation: Cao, W.; Nie, S.; Ma, L.; Zhao, L. Statistical Evaluation of the Performance of Gridded Daily Precipitation Products from Reanalysis Data, Satellite Estimates, and Merged Analyses over Global Land. *Remote Sens.* **2023**, *15*, 4602. https://doi.org/10.3390/rs15184602

Academic Editors: A. K. M. Azad Hossain and Taufique Mahmood

Received: 5 July 2023
Revised: 15 September 2023
Accepted: 16 September 2023
Published: 19 September 2023

1. Introduction

Gridded precipitation datasets are developed and used because they provide detailed knowledge about temporal and spatial representations of precipitation for applications, such as model validation, input for land surface models, as well as extreme rain-event characterization, especially on the global scale. The intensity of the global gridded daily precipitation amount and its spatiotemporal distribution is essential for the global water cycle, the hydrological cycle, the climatic effects of human activities, water resources assessment, and the droughts and floods forecast [1,2].

Gauge observations, satellite estimations, and numerical simulations are three existing principal sources of daily precipitation at the global scale [3]. A series of global gridded

daily or sub-daily precipitation datasets have been designed and produced based on these sources for different applications [4]. Several datasets are based on data sources from sole gauge or satellite observations. Climate Prediction Center (CPC) Unified gauge-based analysis [5], for example, collects gauge observations from more than 30,000 stations over the global land areas, while the Tropical Rainfall Measuring Mission (TRMM) Multi-satellite Precipitation Analysis (TMPA) [6] and CPC's morphing technique (CMORPH) [7] combine precipitation estimates originating from passive microwave (PMW) and infrared (IR) observations from multiple satellite sensors. These datasets reveal the nature of daily precipitation to a certain extent, but they suffer from incomplete global coverage, especially over vast ocean areas and high-latitude areas for gauge- and satellite-based datasets, respectively. The global reanalysis dataset provides an effective way to obtain daily scale precipitation data with complete global coverage. In the several latest global reanalysis datasets, such as the Interim European Center for Medium-Range Weather Forecasts (ECMWF) Re-Analysis (ERA-Interim) [8], the 55 year Japanese Reanalysis Project (JRA-55) [9], and the National Centers for Environmental Prediction (NCEP) Climate Forecast System Reanalysis (CFSR) [10], precipitation is usually produced by a short-range forecast from the operational model, assimilating a wide variety of atmospheric observations but not precipitation measurements. The numerical forecast of precipitation performs well at middle and high latitudes but performs poorly at low latitudes owing to the accumulation of model errors caused by various physical processes [11].

The deficiencies in individual precipitation sources have led to attempts to combine the complementary information of each source to exploit the advantages of each for producing optimal estimations of global fine-scale precipitation with complete global coverage. Two multiple-source merged daily gridded precipitation datasets are available for the study of the global fine-scale water cycle. A widely available global daily precipitation dataset produced by The Global Precipitation Climatology Project (GPCP), called GPCP one-degree daily (GPCP-1DD) [12], is the first product developed for estimating daily precipitation with complete global coverage from multiple sources (daily precipitation information from satellites and monthly precipitation information from gauge analyses). The GPCP-1DD product has been widely used in many fields such as weather process diagnostic analyses, hydrologic streamflow model validation, flood monitoring and forecasting, and climate change applications [13–17].

The Beijing Climate Center of the China Meteorological Administration (BCC/CMA) has crafted a global daily precipitation dataset known as BCC Merged Estimation of Precipitation (BMEP). This dataset amalgamates daily-scale information from gauges, satellites, and reanalysis sources [18]. Notably, BMEP stands as a global gridded precipitation dataset on a daily scale, incorporating inputs from all three primary data sources. Given the advantage of each data source in understanding of the temporal and spatial variability of fine time scale precipitation on a global scale, it is essential to merge information from multiple sources to take advantage of the strengths offered by each type.

At present, there have been numerous comparative evaluations conducted for various gridded precipitation datasets from different sources. Due to the limited availability of daily gridded precipitation with complete global coverage, most comparisons between such datasets have been conducted at regional scales [19–22]. However, comprehensive comparisons between daily gridded precipitation datasets from different sources, particularly multiple-source merged datasets, have been scarce. Beck et al. have utilized original global station precipitation observations for validation [23]. However, due to the uneven distribution of these stations around the world and challenges in assembling the data, these analyses often miss out on regions with sparse or no station coverage. Consequently, they struggle to provide a clear picture of precipitation patterns across the entire global land area. Furthermore, it is worth noting that in previous comparative assessment studies of various global gridded precipitation datasets, there has been limited exploration of products originating from China's developed global grid-based precipitation dataset, e.g., the BMEP dataset. The few available studies have primarily focused on comparing

the monthly-scale BMEP product within China's region [15]. Limited attention has been dedicated to assessing its performance on a global scale and at the daily resolution.

In this study, we extensively compare five gridded daily precipitation datasets (BMEP, GPCP-1DD, JRA-55, ERA-I, CFSR) with complete global coverage and evaluate them using gauge-based analysis of daily precipitation over global land areas (CPC-Unified, referred to as CPC-U). The objective is to assess their reliability in representing the spatial and temporal variability of global daily precipitation and provide recommendations regarding the quality and utilization of these datasets for a comprehensive understanding of global water and hydrological cycles. As BMEP is a recently developed dataset, it is crucial to inform the community about its quality analysis and differences from other global precipitation datasets. Moreover, this evaluation can potentially offer valuable insights for developers of these global precipitation datasets for enhancing their products. By harnessing the strengths of each dataset, researchers and practitioners can enhance the precision and comprehensiveness of global fine-scale precipitation assessment, enabling more effective flood forecasting and simulation capabilities.

2. Data and Methods

2.1. Reanalysis Data

In this study, three recent reanalysis daily precipitation datasets, i.e., ERA-Interim (hereafter ERA-I), JRA-55, and CFSR [8–10], are inter-compared and evaluated at daily and global scales. A wide range of conventional and satellite observations are assimilated using modern techniques in these reanalysis dataset—but, in general, not precipitation measurements. Consequently, reanalysis precipitation is typically produced by the short-range forecast based on atmospheric temperature and humidity information derived from assimilation systems. ERA-I (available from January 1979 to December 2018) and JRA-55 (available from January 1958 to February 2022) utilize four-dimensional variational data assimilation (4DVAR) and apply variational bias correction for satellite radiances [8,9]. CFSR employs three-dimensional variational data assimilation (3DVAR) and considers the flow dependence of background error variances based on grid point statistical interpolation [10]. The initial version of CFSR data covers the period from 1979 to the end of 2010. As NCEP's Climate Forecast System Version 2 (CFSv2) became operational after 2010, the CFSR data are no longer updated. For the period after 2010, datasets for CFSv2 were utilized to extend the CFSR data. This substitution is reasonable because CFSv2 shares similar modeling and assimilation systems with CFSR, and it employs more advanced assimilation techniques [24]. The state-of-the-art model physics as well as the advanced data assimilation method employed in these reanalyses effectively reduce biases and errors, leading to significant improvements in precipitation forecasting skills. The original horizontal resolution of these reanalysis datasets used in this study is ~79 km for ERA-I, 1.25° for JRA-55, and ~38 km for CFSR. The six-hour precipitation data from these reanalysis datasets were aggregated into a daily temporal resolution to facilitate the comparisons of distributions and variability.

2.2. Merged Data

The GPCP-1DD dataset was the first product developed for estimating daily precipitation with complete global coverage from multiple sources [12]. It was produced in 1.0° × 1.0° spatial resolution by merging daily sounding data from low-earth polar-orbit satellites, using the threshold-matched index (TMPI) between 40°S and 40°N and an adjusted TOVS cloud volume proxy outside of this latitude band. The GPCP-1DD was rescaled to align with the monthly GPCP satellite–gauge precipitation estimate [25], which relied on rain gauge analysis from the Global Precipitation Climatology Center (GPCC) [26] on a monthly time scale. Version 1.2 of the GPCP-1DD data provides comprehensive global coverage and spans from January 1996 to October 2015 [27].

The BMEP was a rare daily-scale global gridded precipitation dataset adopting daily precipitation information from gauge, satellite, and numerical model sources by means of a

multiple-step strategy. The gauge observations used in BMEP are exclusively sourced from the Global Telecommunication System (GTS) dataset, covering approximately 15,000 stations globally. Initially, satellite estimates and numerical predictions were adjusted using quality controlled, daily gauge observation data [28] across global land areas. Subsequently, the overall bias in the satellite estimates and numerical predictions over oceanic areas was eliminated through a specific rescaled method using monthly data. Finally, the gauge-adjusted satellite estimates and numerical predictions were merged with the gauge data based on a cumulative distribution function (CDF) bias correction procedure and an objective merging algorithm [29]. The first version of this dataset featured a spatial resolution of 1.0° × 1.0° and complete global coverage. It was available from January 2003 to July 2017 [18].

2.3. Validation Data

Ground-based gauges are commonly considered the most reliable source of precipitation observations [30]. In this study, the CPC-U rain gauge dataset was utilized to evaluate gridded daily precipitation from reanalysis datasets and combined datasets on a global scale. The CPC-U dataset incorporates data from over 30,000 daily and hourly observing stations, including those from the GTS dataset, Cooperative Observer Network, National Climatic Data Center's cooperative dataset, and various national and international agencies. The CPC-U data have a dense network of stations in regions like the United States, Mexico, South America, and Australia, implying higher data quality in these areas [31]. Conversely, regions with sparse station coverage such as the African continent, northern Europe, western China, central Australia, and the Amazon exhibit lower accuracy and higher uncertainty for these regions. Gridded values of daily precipitation in the CPC-U dataset were calculated using a modified Cressman scheme [32], with bias correction applied to account for orographic effects [33]. The CPC-U data are available on a daily basis, with a spatial resolution of 0.5° × 0.5°, spanning from 1979 to 2005. Additionally, a real-time version of CPC-U data based on approximately 17,000 stations is available at the same temporal and spatial resolutions from 2005 to the present. To cover the entire period of this study, a combination of historical and real-time versions of the CPC-U dataset was employed.

2.4. Evaluation Methods

To mitigate the potential impact of varying spatial resolutions, all gridded precipitation datasets used in this study were initially interpolated onto a standardized 1° × 1° grid using the bilinear interpolation method. The evaluation period for this study spanned from January 2003 to December 2016, during which all selected precipitation datasets in this study provide complete annual data coverage. The performance of these gridded daily precipitation datasets was assessed using several key statistical metrics, including the long-term means, spatial and temporal bias characteristics, correlation coefficient (CC), root-mean-square error (RMSE), and interannual variability.

The bias was used to evaluate the average systemic bias between the gridded precipitation datasets and the CPC-U precipitation data in terms of time or space; the RMSE was used to determine the total magnitude of the difference in time or space between the gridded precipitation data and the CPC-U data; and the CC was used to reflect the linear consistency of the temporal or spatial variability between the gridded precipitation data and the CPC-U data. The temporal or spatial values of bias, RMSE, and CC are calculated, respectively, as follows:

$$BIAS = \frac{1}{n}\sum_{1}^{n}(G_i - O_i) \quad (1)$$

$$RMSE = \sqrt{\frac{1}{n}\sum_{1}^{n}(G_i - O_i)^2} \quad (2)$$

$$CC = \frac{\sum_1^n (G_i - \overline{G})(O_i - \overline{O})}{\sqrt{\sum_1^n (G_i - \overline{G})^2} \cdot \sqrt{\sum_1^n (O_i - \overline{O})^2}} \quad (3)$$

where n is the number of days in the entire study period (for temporal metrics) or the number of grid points in the selected spatial region (for spatial metrics), G_i and O_i are the gridded precipitation data and the CPC-U precipitation data at the ith days or grids, respectively, and $\overline{G}$ and $\overline{O}$ are the time-averaged or space-averaged values of G_i and O_i, respectively. These metrics capture the primary temporal and spatial features of daily precipitation.

Additionally, we conducted a comparative analysis of the categorical statistics of these gridded datasets, using gauge observations from the CPC-U dataset, to perform a dichotomous verification of rainfall events.

Based on the standard 2 × 2 contingency table [34], rain events across each grid box can be categorized into four types: hits (H, representing the number of grid boxes with observed rain correctly detected), misses (M, indicating the number of grid boxes with observed rain not detected), false alarms (F, denoting the number of grid boxes without observed rain but detected), and correct no rain (Z, signifying the number of grid boxes with neither observed nor detected rain). To quantify the accuracy of the gridded daily precipitation products in detecting rainfall events, various metrics such as the probability of detection (POD), false alarm ratio (FAR), and equitable threat score (ETS) were calculated for different daily precipitation thresholds across the global land area. The definitions and calculations for these indices were elaborated in detail by Ebert et al. [35]. The concise definitions of these three metrics are as follows:

1. Probability of Detection (POD = H/(H + M)): This index quantifies the fraction of correctly detected rain events out of all observed instances, with values ranging from 0 to 1, and a perfect score denoting 1. It gauges the accuracy of rain event detection.
2. Probability of Detection (POD = H/(H + M)): This index quantifies the fraction of correctly detected rain events out of all observed instances, with values ranging from 0 to 1, and a perfect score denoting 1. It gauges the accuracy of rain event detection.
3. Equitable Threat Score (ETS = (H − G)/(H + M + F − G)), where G = (H + M) (H + F)/N): The ETS provides a balanced assessment by considering the random chance. It considers both hits and false alarms in relation to what could occur by random chance alone.

3. Results

3.1. Spatial Distribution of Annual Means

Figure 1 illustrates the spatial distribution of multi-year mean daily precipitation across the globe from 2003 to 2016. The gauge-based CPC-U data show that the highest annual mean precipitation areas over global land are in the Indonesian Islands (over 7 mm/d) situated within the western tropical Pacific ITCZ region. Additionally, the Amazon (over 5 mm/d) and Equatorial Africa (over 3 mm/d) represent two distinct rainfall centers influenced by the expansion of the eastern Pacific ITCZ. The eastern coastal regions of Asia (over 4 mm/d) and North America (over 3 mm/d) exhibit high precipitation levels associated with mid-latitude storm tracks. All reanalysis datasets and combined datasets successfully capture the overall spatial distribution of CPC-U's annual mean precipitation across the globe. However, GPCP-1DD, ERA-I, CFSR, and JRA-55 show a significant overestimation of precipitation over the Amazon rainfall center. GPCP-1DD and CFSR also overestimate precipitation over the Kalimantan Islands, while BMEP, ERA-I, and JRA-55 underestimate it. Other gridded datasets, except BMEP, substantially overestimate rainfall centers over New Guinea Island, eastern coastal regions of China, and the Bay of Bengal. Although all gridded datasets detect the rainfall belt over Equatorial Africa, there are notable differences in the locations and magnitudes of the strong rainfall center among these precipitation estimates.

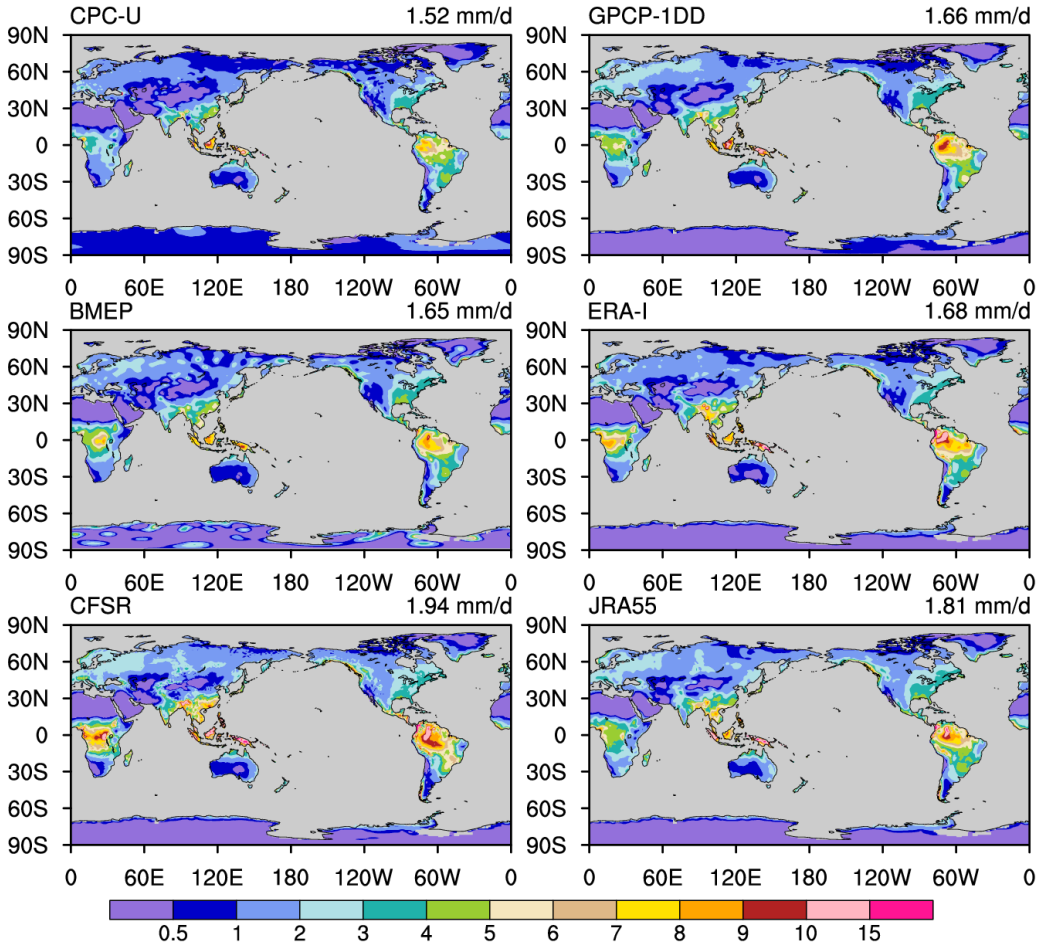

Figure 1. The spatial distribution of multi-year mean daily precipitation (mm/d) for CPC-U, GPCP-1DD, BMEP, ERA-I, CFSR, and JRA-55 datasets during the period 2003–2016. (The value in the upper right corner of each subfigure is the global mean value).

3.2. Statistical Indices

3.2.1. Bias

The spatial distributions of the multi-year mean of daily precipitation bias from each gridded dataset against CPC-U data are presented in Figure 2. Notably, a consistent tendency to overestimate the annual mean precipitation emerges in specific regions. Equatorial Africa, for instance, exhibits an overestimation exceeding 3 mm/d, while the Amazon and the Indo-China Peninsula both show overestimations exceeding 2 mm/d. Conversely, in numerous parts of northern Eurasia (above 30°N), northern Africa, Australia, and North America, the biases are smaller in magnitude, ranging between −0.5 mm/d and 0.5 mm/d. Remarkably, except for ERA-I, reanalysis products exhibit more extensive large-scale patterns of bias, a trend that extends further when contrasted with the merged products of BMEP and GPCP-1DD. This is especially pronounced in areas characterized by lower annual mean daily precipitation, as illustrated in Figure 1.

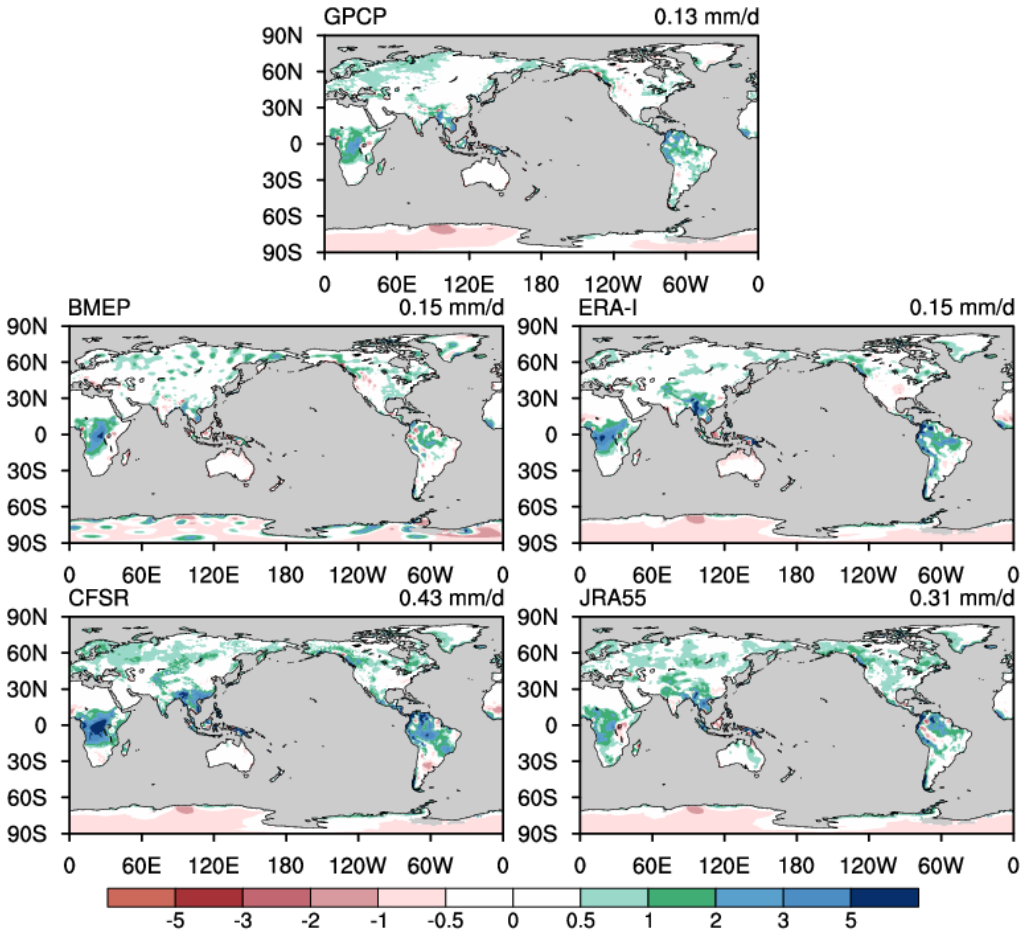

Figure 2. The spatial distribution of the multi-year mean of daily precipitation bias from each gridded dataset against CPC-U data during the period 2003–2016. (The value in the upper right corner of each subfigure is the global mean value).

3.2.2. Time Correlation Coefficient (TCC)

Figure 3 presents the spatial distributions of the multi-year mean of the daily precipitation TCC for each gridded dataset in comparison to the CPC-U data. Notably, BMEP exhibits a notably enhanced performance in terms of spatial patterns and TCC values when juxtaposed with other gridded precipitation products, particularly in regions endowed with a more densely distributed network of gauge observations [18]. In contrast, GPCP-1DD, despite relying on gauge-based precipitation observations [12], exhibits diminished TCC values compared to the three reanalysis datasets that do not encompass direct precipitation observations. This could be attributed to the fact that BMEP uniquely integrates daily gauge precipitation information during its creation process [18], thereby enhancing its ability to capture the fine-scale temporal variations in precipitation. On the other hand, the three reanalysis datasets adjust precipitation predictions through the assimilation of various atmospheric observational data from their respective systems [8–10]. However, in the case of GPCP-1DD, the monthly gauge-based precipitation analysis data sourced from GPCP-SG [12] falls short in capturing the intricacies of daily-scale precipitation variability, thereby underscoring the limitations of its performance in this context.

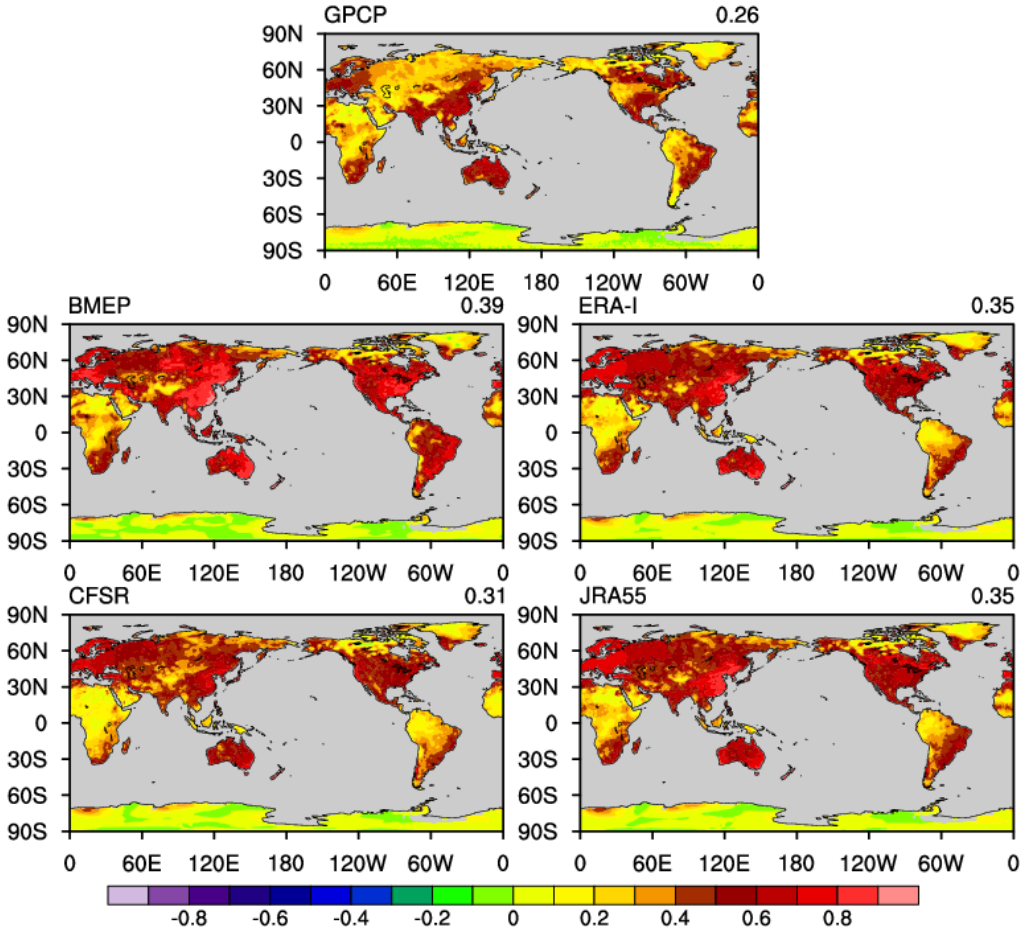

Figure 3. The spatial distribution of the multi-year mean of the daily precipitation time correlation coefficient from each gridded dataset against CPC-U data during the period 2003–2016. (The value in the upper right corner of each subfigure is the global mean value).

3.2.3. RMSE

The spatial distributions of the multi-year mean of daily precipitation RMSE from each gridded dataset against CPC-U data are meticulously detailed in Figure 4. It is worth noting that the spatial patterns of RMSE observed across all gridded datasets (as illustrated in Figure 2) are in accord with those of annual means (as depicted in Figure 1). This alignment echoes findings from previous studies [22,36] that have underscored the inherent correlation between the magnitude of precipitation and the associated error in fine-scale precipitation representations. It is particularly noteworthy that the prominently high RMSE region over the Antarctic continent does not arise from inaccuracies in rainfall intensity estimates derived from gridded precipitation datasets. Notably, the notable area of elevated RMSE values across the Antarctic continent is not the result of inaccuracies in rainfall intensity estimation stemming from the gridded precipitation products themselves. Instead, it can be attributed to the original interpolation errors present in the CPC-U data, a crucial context not explicitly depicted in the figure. These results enhance our comprehension of the intricate factors contributing to spatial discrepancies and errors within gridded precipitation datasets.

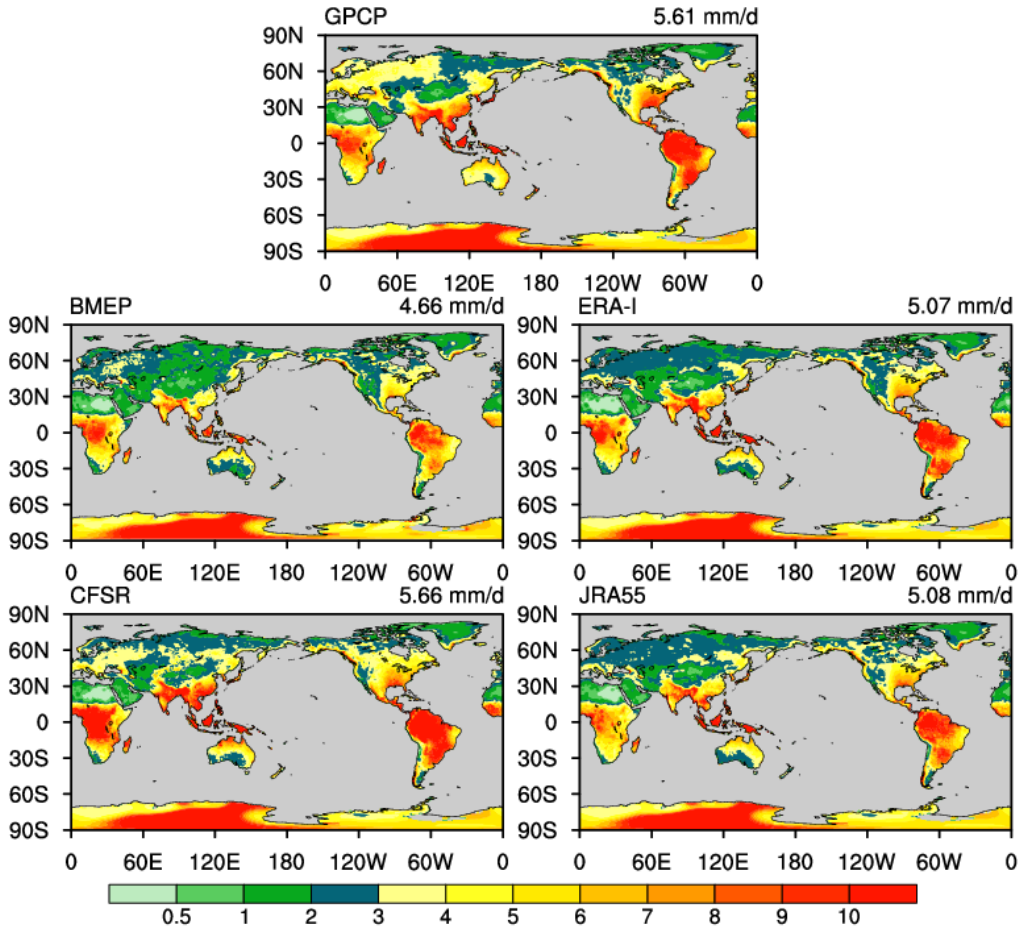

Figure 4. The spatial distribution of the multi-year mean of daily precipitation RMSE from each gridded dataset against CPC-U data during the period 2003–2016. (The value in the upper right corner of each subfigure is the global mean value).

Table 1 summarizes the globally averaged statistics for each dataset. The annual mean precipitation ranges from 1.65 mm/d (BMEP) to 1.94 mm/d (CFSR) among the gridded datasets, indicating a 9% (BMEP) and 28% (CFSR) higher estimate compared to CPC-U data. Among the datasets, GPCP-1DD and BMEP exhibit the smallest overall bias. Notably, BMEP exhibits an overall advantage over other gridded datasets in other statistical measures, with the smallest RMSE and the largest TCC. This highlights the significant improvements achieved by merging data from multiple sources in estimating daily precipitation. Conversely, GPCP-1DD demonstrates inferior TCC and RMSE performance compared to BMEP, ERA-I, and JRA-55, despite also being a merged dataset. The results for reanalysis products are mixed, with CFSR exhibiting higher bias and RMSE errors compared to all other datasets, while ERA-I and JRA-55 demonstrate more favorable TCC (both 0.35) and RMSE (both around 5.07 mm/d) performances, even surpassing the merged data from GPCP-1DD.

Table 1. The global averaged multi-year averages for annual means (AM, mm/d), biases (mm/d), time correlation coefficients (TCC), and RMSEs (mm/d) of daily precipitation for each daily precipitation dataset during the period 2003–2016.

Indexes	CPC-U	GPCP-1DD	BMEP	ERA-I	CFSR	JRA55
AM	1.52	1.66	1.65	1.68	1.94	1.81
Bias	-	0.13	0.15	0.15	0.43	0.31
TCC	-	0.26	0.39	0.35	0.31	0.35
RMSE	-	5.61	4.66	5.07	5.66	5.08

3.3. Time Series of Regional Means

The time series of the global averaged daily precipitation intensity between gridded datasets and CPC-U over global, northern hemisphere, and southern hemisphere land areas are shown in Figure 5. The interannual variability of daily precipitation is consistent among all datasets with the annual cycle of CPC-U observations, which could be caught by all five gridded datasets over the global land area (Figure 5a). The global land average and the Northern Hemisphere land average exhibit congruent annual cycles of daily precipitation. The peak of precipitation is observed during the months of July and August, while the lowest values occur around January. In contrast, the annual cycle in the Southern Hemisphere land regions presents a precisely opposite pattern, with peak precipitation occurring around January and trough values appearing in July and August. Analyzing the consistency between different precipitation datasets, specifically the CPC-U precipitation and other products, reveals that the datasets demonstrate superior consistency in the average time series of both hemispheres compared to the global land average. Notably, the dispersion among the datasets is significantly greater in the global average than in the hemisphere-specific results.

Throughout the evaluation period, the temporal curves of precipitation in the BMEP dataset closely align with those of the CPC-U product in the Southern Hemisphere. Conversely, alternative precipitation products such as GPCP-1DD, ERA-I, JRA-55, and CFSR display noticeable positive biases in precipitation intensity when compared to both BMEP and CPC-U data throughout the entire period. This positive bias is not particularly pronounced during the annual precipitation troughs but becomes more distinct during the periods of the annual precipitation peak. Also, the positive bias is primarily concentrated within the Equatorial region (the figure has not been presented). The overestimation of precipitation over the Equatorial region in reanalysis data, such as ERA-I, may be attributed to an overestimation of the deep convection and moisture flux convergence over the tropical land [37]. This issue is likely a common challenge across other reanalysis precipitation products. The overestimation of Equatorial precipitation in the GPCP-1DD dataset could potentially stem from the incorporation of the monthly average GPCP-SG gridded data for the correction of daily precipitation values during its production process [12]. It is generally recognized that monthly average precipitation data possess greater spatial integrity compared to daily precipitation data. Consequently, utilizing monthly averages to amend daily averages may inadvertently result in an overestimation of cumulative daily precipitation values.

In the Northern Hemisphere, both BMEP and ERA-I products exhibit positive biases compared to CPC-U data. A possible explanation for this phenomenon is that CPC-U data rely solely on station observations, whereas BMEP or ERA-I data incorporate satellite or reanalysis data as well. In regions with sparse station coverage, CPC-U assigns a value of 0 to grid points without station observations, whereas BMEP or ERA-I data often incorporate satellite-derived or reanalysis-based precipitation in those grid points, leading to values greater than 0. Consequently, in areas with limited station coverage, the values of BMEP and ERA-I data tend to be higher compared to the CPC-U data.

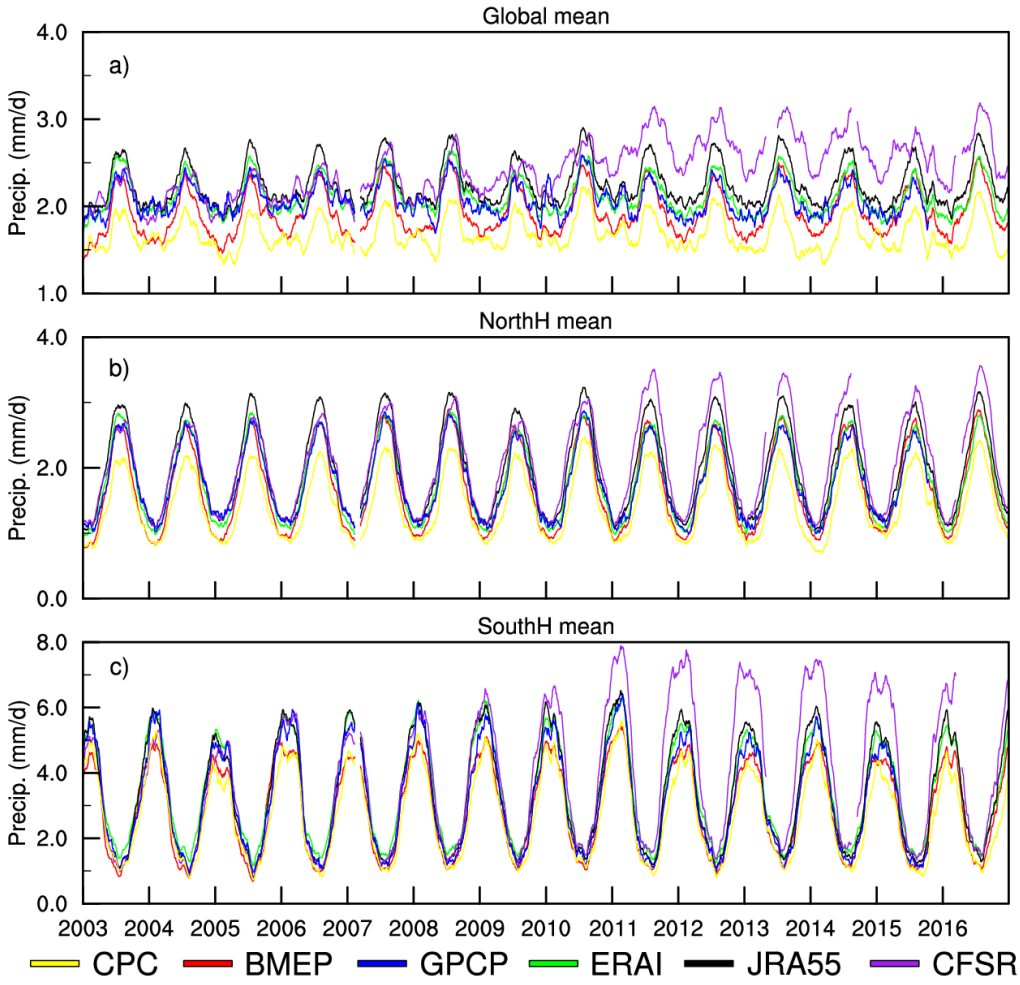

Figure 5. The time series of daily precipitation over the (**a**) global land area (60°S–90°N), (**b**) northern hemisphere land area (0°N–90°N), and (**c**) southern hemisphere land area (60°S–0°S) for CPC-U data and each gridded daily precipitation datum from 2003 to 2016. (A 31-point smoothing was applied to all lines to enhance the distinguishability of the lines).

It is noteworthy that the CFSR data exhibit a notable positive trend from 2003 to 2016, particularly after 2011, which is not observed in other datasets. This divergence can be attributed to the transition from CFSR data to CFSv2 data. While the modeling and assimilation systems used in CFSv2 are quite similar to those of CFSR, there are still certain differences between CFSv2 as an operational system and the CFSR reanalysis system [38]. On one hand, CFSv2 employs a new gravity wave parameterization scheme [38], based on cumulus convection-induced gravity wave drag, which might lead to an excessive simulation of convective precipitation. On the other hand, being an operational system in real-time, CFSv2 exhibits weaker completeness and quality control of observational data collection compared to the comprehensive reanalysis system of CFSR, which to some extent affects the accuracy of precipitation forecasting. These two factors could potentially result in noticeable differences in precipitation in the CFSR data after the period of 2010. This abnormal bias in the CFSR data aligns with previous research indicating that the renewal of modeling systems and data assimilation systems can introduce spurious trends in precipitation forecasts, impacting the accuracy of reanalysis-based precipitation assessments [20,39].

3.4. Spatial Biases

Figure 6 illustrates the time series of spatial biases between various grid-based daily precipitation products and the CPC-U precipitation data across global land areas as well as

two hemispheric land areas. The time series of spatial bias exhibit distinct annual cyclic characteristics, mirroring those of the daily precipitation patterns themselves. Furthermore, the annual cyclic features of the spatial bias align closely with the corresponding annual cyclic characteristics of the regional daily precipitation. Specifically, the peak values of the spatial bias curve correspond to the peak values of the average precipitation in each area, while the trough values align with the corresponding minimum precipitation values. The spatial bias of the JRA-55 data is lower than that of the CFSR data but higher than that of other grid-based precipitation datasets. Its larger spatial bias values, compared to other datasets, primarily occur during peak periods (approximately 1.0 mm/d) and remain relatively stable throughout the entire statistical period, without exhibiting the increasing trend observed in the later stages, as observed in the CFSR data.

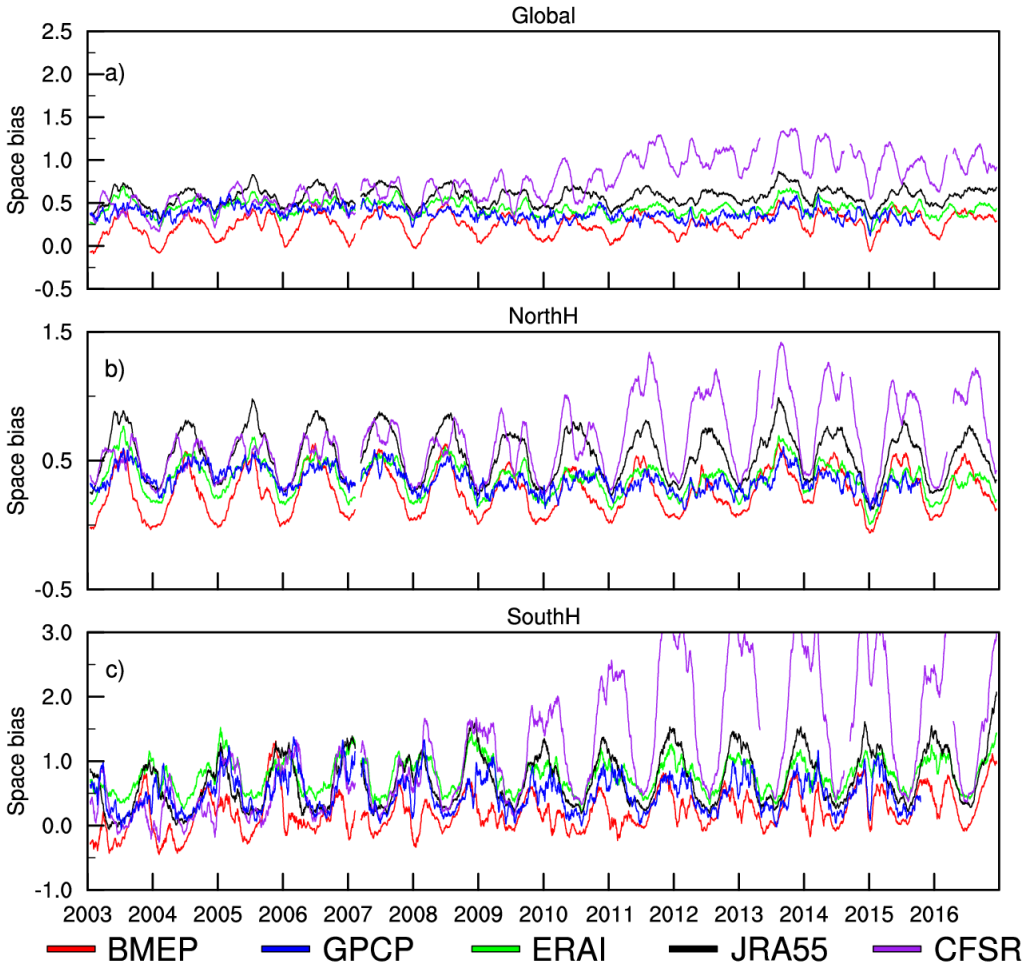

Figure 6. The time series of spatial bias between CPC-U data and each gridded daily precipitation datum from 2003 to 2016 over the (**a**) global land area (60°S–90°N), (**b**) northern hemisphere land area (0°N–90°N), and (**c**) southern hemisphere land area (60°S–0°S). (A 31-point smoothing was applied to all lines to enhance the distinguishability of the lines).

Among these grid-based daily precipitation datasets considered, the BMEP precipitation showcases the smallest spatial bias characteristics across global land areas and two hemispheric land areas (Table 2). Specifically, within global land areas, the BMEP data exhibit an average spatial bias reduction of over 0.13 mm/d compared to other datasets. Notably, in the Southern Hemisphere land areas, the average spatial bias of the BMEP data demonstrates a substantial reduction of approximately 1 mm/d in comparison to the CFSR precipitation. Within global land regions and Northern Hemisphere land regions, the advantages of the BMEP data over alternative precipitation datasets primarily manifest

during the trough periods of the time series, particularly in winter seasons, where the regional average spatial bias remains near zero. However, in the Southern Hemisphere, the spatial bias of the BMEP data does not exhibit a similar characteristic. Nonetheless, it is worth emphasizing that the BMEP data consistently exhibit the smallest regional average spatial bias among these grid-based precipitation products.

Table 2. The time averaged spatial biases (mm/d), spatial correlation coefficients, and spatial RMSEs (mm/d) for each daily precipitation dataset compared to the CPC-U data over the global land area (60°S–90°N), the northern hemisphere (N.H.) land area (0°N–90°N), and the southern hemisphere (S.H.) land area (60°S–0°S) during the period 2003–2016.

Indexes	GPCP-1DD	BMEP	ERA-I	CFSR	JRA55
Spatial bias (global)	0.38	0.25	0.44	0.75	0.57
Spatial corr. (global)	0.42	0.61	0.48	0.44	0.52
Spatial RMSE (global)	5.59	4.27	5.11	6.14	4.90
Spatial bias (N.H.)	0.35	0.26	0.36	0.65	0.54
Spatial corr. (N.H.)	0.40	0.62	0.52	0.48	0.55
Spatial RMSE (N.H.)	4.81	3.57	4.20	4.97	4.09
Spatial bias (S.H.)	0.49	0.21	0.78	1.18	0.70
Spatial corr. (S.H.)	0.39	0.56	0.40	0.36	0.44
Spatial RMSE (S.H.)	7.47	5.83	7.17	8.63	6.74

3.5. Spatial Correlation Coefficients

Figure 7 illustrates the temporal variations of spatial correlation coefficients between different grid-based precipitation products and the CPC-U precipitation data in global land areas and the two hemispheric land areas. Notably, unlike spatial bias, the temporal curves of spatial correlation coefficients exhibit diverse patterns without consistent annual cyclic characteristics. In the global land area (Figure 7a), the spatial correlation coefficients of grid-based precipitation products display minimal evidence of an annual cyclic pattern. However, in the Northern Hemisphere land area, BMEP, ERA-I, JRA-55, and CFSR data demonstrate a coherent yet relatively weak annual cyclic feature in their spatial correlation coefficient curves. Conversely, GPCP-1DD data deviate from this trend, displaying an inconsistent annual cyclic characteristic and exhibiting the lowest spatial correlation coefficient compared to other grid-based precipitation datasets. Due to data gaps in the GPCP-1DD dataset during certain periods in the high-latitude regions of the Northern Hemisphere (40°N–90°N), this leads to significantly lower spatial correlation coefficients between GPCP-1DD and CPC-U during those time intervals. This discrepancy, in turn, leads to a change in the annual cycle for those years on the average curve of the GPCP-1DD spatial correlation coefficient in the North Hemisphere. In the Southern Hemisphere land region, all precipitation datasets exhibit a relatively consistent annual cyclic pattern in the spatial correlation coefficients, with GPCP-1DD data aligning well with the other datasets, demonstrating good consistency.

The BMEP data demonstrate a clear advantage in terms of spatial correlation coefficients compared to other grid-based precipitation products. On a global land average, the spatial correlation coefficients of BMEP data remain consistently above 0.6, significantly higher than those of JRA-55 (0.52), ERA-I (0.48), GPCP-1DD (0.42), and CFSR (0.44). In both the global land area and the Northern Hemisphere land area, JRA-55 precipitation data exhibit higher spatial correlation coefficients compared to ERA-I, CFSR reanalysis data, and GPCP-1DD data. Meanwhile, in the Southern Hemisphere, JRA-55 and ERA-I data display similar levels of spatial correlation coefficients, outperforming GPCP-1DD and CFSR data, with CFSR data exhibiting the poorest performance in terms of spatial correlation coefficients.

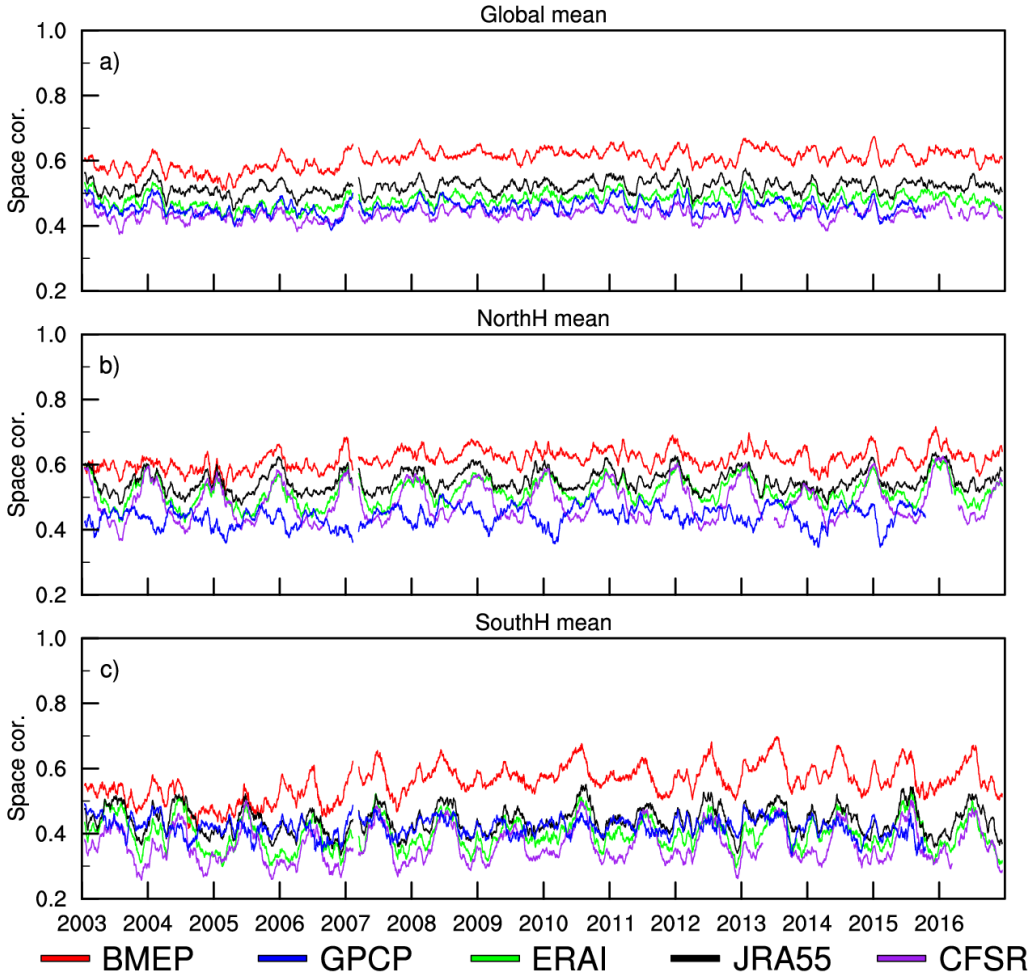

Figure 7. The time series of the spatial correlation coefficient between CPC-U data and each gridded daily precipitation datum from 2003 to 2016 over the (**a**) global land area (60°S–90°N), (**b**) northern hemisphere land area (0°N–90°N), and (**c**) southern hemisphere land area (60°S–0°S). (A 31-point smoothing was applied to all lines to enhance the distinguishability of the lines).

The above results indicate that, in terms of the spatial pattern of global daily precipitation, the BMEP precipitation exhibits the highest spatial consistency with CPC-U precipitation data based on daily station observations. This consistency is evident across the entire global land area and both hemispheric regions at different temporal scales, demonstrating robustness. We speculate that this coherence is attributed to the incorporation of daily station-based precipitation observations in the BMEP data, which is unique among these analyzed datasets. The introduction of more accurate precipitation observations at the daily scale plays a crucial role in improving the temporal variability of grid-based precipitation, thereby positioning BMEP precipitation as the superior product among these examined grid-based precipitation datasets.

3.6. Spatial RMSEs

Figure 8 illustrates the temporal evolution of the spatial RMSE (Root Mean Square Error) for various grid-based precipitation products in comparison to the CPC-U precipitation data across the global land area and the two hemispheric land areas. It is evident that each daily grid-based precipitation dataset exhibits pronounced annual cyclic variations in spatial RMSE within the hemispheric land areas. Notably, the Northern Hemisphere land area and the Southern Hemisphere land area exhibit precisely opposite patterns in their annual cyclic behavior. In the Northern Hemisphere, the peak values of spatial RMSE, relative to the CPC-U data, are observed during the months of July and August, while the

trough values occur around January. Conversely, the Southern Hemisphere land region shows an inverse behavior, with peak spatial RMSE values occurring around January and trough values occurring around July and August. This distinct annual cyclic characteristic of spatial RMSE coincides remarkably with the annual cyclic patterns of precipitation in these areas, emphasizing that the magnitude of spatial RMSE between different grid-based precipitation datasets and the CPC-U data is primarily governed by the intensity of their precipitation amounts.

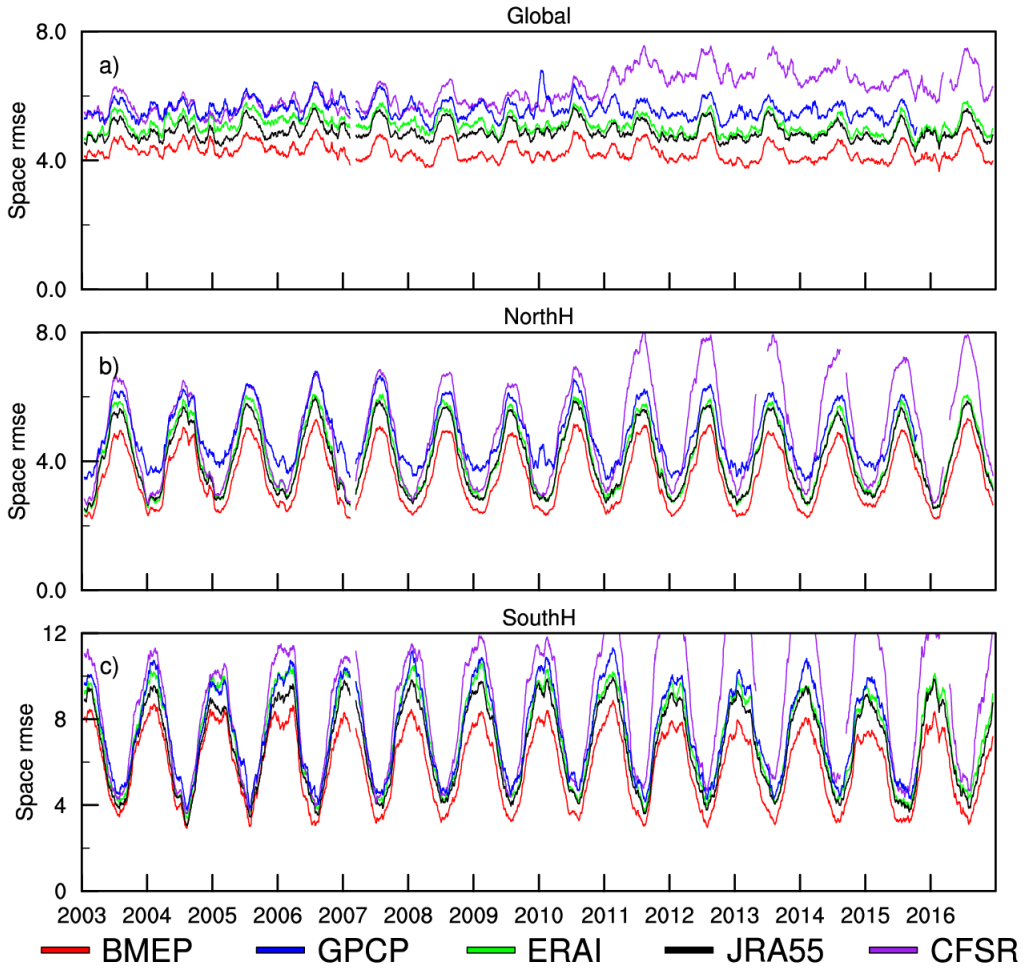

Figure 8. The time series of spatial RMSE between CPC-U data and each gridded daily precipitation datum from 2003 to 2016 over the (**a**) global land area (60°S–90°N), (**b**) northern hemisphere land area (0°N–90°N), and (**c**) southern hemisphere land area (60°S–0°S). (A 31-point smoothing was applied to all lines to enhance the distinguishability of the lines).

The spatial RMSE of BEMP precipitation data is significantly smaller than that of other grid-based daily precipitation datasets in all these analyzed land areas. For the global land average, the time-mean spatial RMSE of BEMP data remains stable at around 4 mm/d (average of 4.27 mm/d, Table 2), which is notably lower than other reanalysis or satellite merged grid-based precipitation datasets. Moreover, the advantage of BEMP data over other grid-based precipitation datasets is consistently evident throughout the entire study period, indicating the robustness of this advantage in terms of spatial RMSE. This is partly attributed to the incorporation of station-based daily precipitation observations in BEMP precipitation data and partly to the implementation of an objective error estimation algorithm that dynamically adjusts the error structure of each merged data source adaptively [29]. Consequently, the errors are effectively reduced, resulting in an outstanding performance of BEMP data compared to other grid-based precipitation datasets.

Additionally, it is noteworthy that despite being a reanalysis-based precipitation product, JRA-55 data demonstrate a spatial RMSE performance that is only surpassed by that of BEMP data. Its average spatial RMSE over the global land, Northern Hemisphere, and Southern Hemisphere land areas is 4.90 mm/d, 4.09 mm/d, and 6.74 mm/d, respectively (Table 2). These values are significantly better than those of ERA-I and CFSR, two widely used reanalysis datasets, and also outperform the satellite-derived merged GPCP-1DD (with average spatial RMSE values of 5.59 mm/d for the global land, 4.81 mm/d for the Northern Hemisphere land, and 7.47 mm/d for the Southern Hemisphere land, as shown in Table 2). These findings indicate that, when it comes to daily precipitation estimation on a global scale, the advantages of GPCP-1DD precipitation based on satellite data are not distinctly evident compared to reanalysis precipitation. Despite the reanalysis precipitation products offering six-hour forecasted precipitation, insufficient handling of satellite precipitation errors in GPCP-1DD can potentially result in greater daily-scale precipitation RMSE compared to reanalysis precipitation products.

3.7. Categorical Statistics

Figure 9 presents the results of POD, FAR, and ETS for five different gridded products across varying daily precipitation thresholds. As the thresholds increase, all gridded products consistently exhibit a decrease in POD and an increase in FAR values. This finding aligns with earlier studies [22,35,40] indicating that identifying heavy rainfall is more challenging than detecting light rain for both merged and reanalysis precipitation products. When considering thresholds ranging from 0.1 to 10 mm/day, BMEP, JRA-55, and CFSR clearly outperform GPCP-1DD in detecting rain occurrence (Figure 9a). Furthermore, the skill of GPCP-1DD deteriorates at a slower rate compared to that of BMEP, JRA-55, and CFSR, resulting in higher POD values for thresholds exceeding 20 mm/d. The FAR of BMEP remains relatively stable around 0.55, significantly lower than that of other datasets for thresholds exceeding 5 mm/d. Conversely, the FAR values of GPCP-1DD and CFSR rapidly escalate, exhibiting substantially higher levels than other gridded data (Figure 9b). These findings highlight BMEP's ability to achieve the lowest false alarm ratios in detecting medium to high precipitation rates across global land areas. To assess the overall capability of detecting rain events, the ETS is evaluated. BMEP exhibits an increasing trend in ETS scores for light rainfall events, reaching its peak at a threshold of 5 mm/d. Moreover, BMEP consistently maintains significantly higher ETS scores than other products, gradually declining as the threshold increases (Figure 9c). The superior performance of BMEP in ETS scores can be attributed to its substantially lower number of false alarms. This indicates that BMEP excels in successfully identifying daily precipitation, particularly for moderate and heavy rain events.

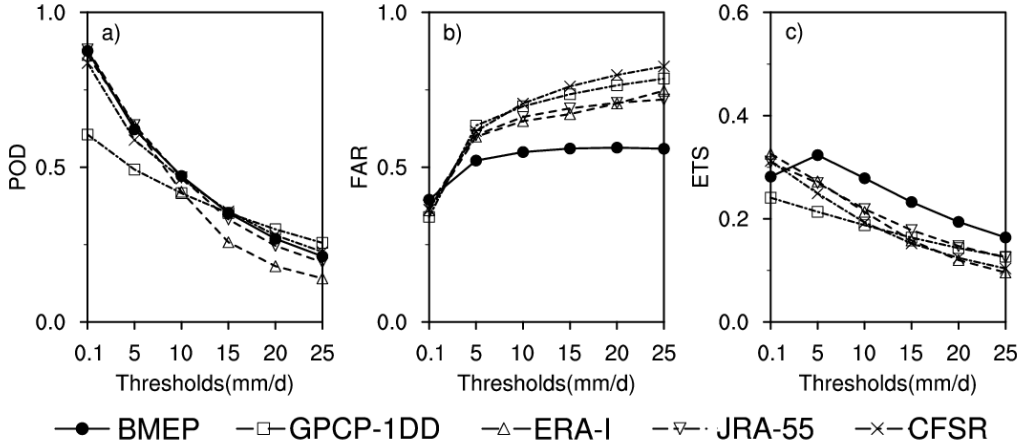

Figure 9. Statistical indices of daily precipitation from BMEP, GPCP-1DD, ERA-I, JRA-55, and CFSR versus CPC-U for POD, FAR, and ETS at different precipitation thresholds.

4. Conclusions

In this study, the performance of five daily-scale gridded precipitation datasets with complete global coverage including BMEP, GPCP-1DD, ERA-interim, JRA-55, and CFSR over a global land area have been systematically compared with the CPC-Unified gauge-based data during the period of 2003–2016 in terms of the annual mean, daily time series, spatial and temporal characteristics of bias, CC, and RMSE, as well as the POD, FAR, and ETS of the occurrence of rainfall events for different daily precipitation thresholds.

1. Gauge-based CPC-U data show that the Indonesian Islands have the highest annual mean precipitation over global land. The Amazon, Equatorial Africa, eastern coastal regions of Asia, and North America also experience significant rainfall. Reanalysis and merged datasets capture the overall precipitation patterns, but some datasets exhibit overestimation or underestimation in specific regions.
2. Gridded datasets tend to overestimate precipitation in Equatorial Africa, the Amazon, and the Indo-China Peninsula. Among the reanalysis products, ERA-I and JRA-55 perform well in terms of correlation coefficients and RMSE. GPCP-1DD and BMEP exhibit the smallest overall bias. BMEP exhibits an overall advantage over other gridded datasets in other statistical measures, with the smallest RMSE and the largest TCC. Conversely, GPCP-1DD underperforms compared to BMEP, ERA-I, and JRA-55. Overall, BMEP shows substantial advantages, while CFSR exhibits notable biases and RMSE errors.
3. The interannual variability of daily precipitation is consistent across all datasets, with the annual cycle captured by the five gridded datasets over global land areas. Peak precipitation occurs in July and August in the Northern Hemisphere, while the Southern Hemisphere exhibits an inverse pattern with peak precipitation in January. The datasets demonstrate better agreement within each hemisphere compared to the global average. BMEP and CPC-U data exhibit remarkable consistency, with BMEP demonstrating superior performance compared to other gridded products on a global scale and in both hemispheres. However, GPCP-1DD, ERA-I, and JRA-55 display noticeable positive biases in precipitation intensity compared to CPC-U. The CFSR data show a notable positive trend after 2011, attributed to the transition from CFSR data to CFSv2 after the year 2010. CFSv2's new gravity wave parameterization for cumulus convection-induced drag may cause excess convective precipitation, and its real-time operational nature affects observational data quality, potentially impacting precipitation accuracy after 2010. This finding aligns with previous research suggesting that updates of modeling systems and data assimilation systems can introduce spurious trends in precipitation forecasts, impacting the accuracy of reanalysis-based assessments.
4. The spatial bias in daily precipitation exhibits distinct annual cyclic patterns, reflecting the true precipitation dynamics. Among the analyzed datasets, BMEP demonstrates the smallest global and hemispheric spatial bias, surpassing others by a notable margin. Moreover, BMEP showcases exceptional spatial consistency with CPC-U precipitation data, boasting superior global and hemispheric spatial correlation coefficients. This remarkable performance is attributed to the incorporation of daily station-based precipitation observations, enhancing the temporal variability of grid-based precipitation estimates. Additionally, BMEP consistently outperforms its counterparts in terms of spatial RMSE, maintaining a stable value of around 4 mm/d for the global land average. Notably, satellite-based GPCP-1DD precipitation does not exhibit distinct advantages over reanalysis precipitation for global daily estimation, and caution should be exercised during the use of these datasets. JRA-55 stands out as a reliable alternative that exhibits competitive performance, outshining widely used reanalysis datasets and the satellite-derived GPCP-1DD.
5. The performance of gridded precipitation products varies with precipitation thresholds. As the thresholds increase, the probability of detecting rainfall decreases (lower POD), while the false alarm ratio increases (higher FAR). BMEP, JRA-55, and CFSR

outperform GPCP-1DD in detecting rain occurrence for thresholds ranging from 0.1 to 10 mm/d. Among them, BMEP consistently exhibits the lowest FAR, especially for thresholds above 5 mm/d, indicating its superiority in detecting moderate to heavy precipitation over global land areas. The ETS analysis demonstrates that BMEP achieves higher scores for light rainfall events and maintains superior performance across different thresholds. This is primarily due to its significantly lower false alarm rate, highlighting BMEP's effectiveness in accurately detecting daily precipitation, particularly for moderate and heavy rain events.

This study demonstrates that BMEP precipitation, which incorporates daily station observations, exhibits significant advantages over other global gridded products at the daily scale, providing a more reasonable and accurate characterization of global precipitation. The findings of this study provide an initial assessment of the temporal and spatial error characteristics of widely used global daily precipitation gridded datasets. These results can offer valuable feedback to developers for improving their precipitation products and serve as useful references for users of these datasets.

We suggest that further work should address this area. Specifically, detailed evaluations should be conducted on the performance of daily gridded precipitation at smaller scales, as well as its performance in numerical modeling, hydrological monitoring and forecasting, flood prediction, and early warning systems. Understanding the strengths and weaknesses of various reanalysis and merged daily precipitation datasets in terms of these aspects will contribute to better support for global flood simulation, hydrological monitoring, and geological hazard early warning. Additionally, future studies could also explore the potential integration of other observational datasets, such as remote sensing and radar data, to further improve the accuracy and coverage of global precipitation estimates. Continuous efforts in advancing data merged techniques and improving quality control procedures would also enhance the reliability and usability of global gridded precipitation datasets.

Author Contributions: Conceptualization, W.C. and S.N.; methodology, W.C.; formal analysis, W.C. and S.N.; validation, W.C. and L.M.; investigation, L.M. and L.Z.; resources, W.C. and S.N.; data curation, W.C., S.N. and L.Z.; writing—original draft preparation, W.C.; writing—review and editing, W.C. and S.N.; visualization, W.C. and L.M.; project administration, S.N.; funding acquisition, W.C., S.N. and L.Z. All authors have read and agreed to the published version of the manuscript.

Funding: This research was funded by the National Natural Science Foundation of China (grant nos. 42275175 and 41801022), the Beijing Natural Science Foundation (grant no. 8192016), the Guangdong Major Project of Basic and Applied Basic Research (2020B030103004), and the Strategic Priority Research Program of the Chinese Academy of Sciences (XDA23090102).

Data Availability Statement: Publicly available datasets were analyzed in this study. The CPC-U data can be found here: https://climatedataguide.ucar.edu/climate-data/cpc-unified-gauge-based-analysis-global-daily-precipitation (accessed on 1 September 2023); the GPCP-1DD data can be found here: ftp.ncdc.noaa.gov//pub/data/gpcp/ (accessed on 1 September 2023); the BMEP data can be found here: http://bcc.ncc-cma.net/channel.php?channelId=132 (accessed on 1 September 2023); the CFSR data can be found here: https://rda.ucar.edu/datasets/ds093.0/ (accessed on 1 September 2023); the CFSv2 data can be found here: https://rda.ucar.edu/datasets/ds094.0/ (accessed on 1 September 2023); the ERA-I data can be found here: https://www.ecmwf.int/en/forecasts/dataset/ecmwf-reanalysis-interim (accessed on 1 September 2023); the JRA-55 data can be found here: https://rda.ucar.edu/datasets/ds628.0/ (accessed on 1 September 2023).

Conflicts of Interest: The authors declare no conflict of interest.

References

1. Gruber, A.V.; Levizzani, V. *Assessment of Global Precipitation, a Project of the Global Energy and Water Cycle Experiment (GEWEX) Radiation Panel, World Climate Research Program*; GEWEX/WCRP Report; WMO: Geneva, Switzerland, 2006; pp. 4–7.
2. Kucera, P.; Ebert, E.; Turk, F.; Levizzani, V.; Kirschbaum, D.; Tapiador, F.; Loew, A.; Borsche, M. Precipitation from Space: Advancing Earth System Science. *Bull. Am. Meteorol. Soc.* **2013**, *94*, 365–375. [CrossRef]

3. Michaelides, S.; Levizzani, V.; Anagnostou, E.; Bauer, P.; Kasparis, T.; Lane, J.E. Precipitation: Measurement, remote sensing, climatology and modeling. *Atmos. Res.* **2009**, *94*, 512–533. [CrossRef]
4. National Center for Atmospheric Research Staff. The Climate Data Guide: Precipitation Data Sets: Overview & Comparison Table. Available online: https://climatedataguide.ucar.edu/climate-data/precipitation-data-sets-overview-comparison-table (accessed on 5 July 2023).
5. Chen, M.; Shi, W.; Xie, P.; Silva, V.B.S.; Kousky, V.E.; Wayne Higgins, R.; Janowiak, J.E. Assessing objective techniques for gauge-based analyses of global daily precipitation. *J. Geophys. Res.* **2008**, *113*, D04110. [CrossRef]
6. Huffman, G.J.; Bolvin, D.T.; Nelkin, E.J.; Wolff, D.; Adler, R.; Gu, G.; Hong, Y.; Bowman, K.; Stocker, E. The TRMM Multisatellite Precipitation Analysis (TMPA): Quasiglobal, multiyear, combined-sensor precipitation estimates at fine scales. *J. Hydrometeorol.* **2007**, *8*, 38–55. [CrossRef]
7. Joyce, R.J.; Janowiak, J.E.; Arkin, P.A.; Xie, P. CMORPH: A method that produces global precipitation estimates from passive microwave and infrared data at high spatial and temporal resolution. *J. Hydrometeorol.* **2004**, *5*, 487–503. [CrossRef]
8. Dee, D.P.; Uppala, S.M.; Simmons, A.J.; Berrisford, P.; Poli, P.; Kobayashi, S.; Andrae, U.; Balmaseda, M.A.; Balsamo, G.; Bauer, D.P.; et al. The ERA-Interim reanalysis: Configuration and performance of the data assimilation system. *Q. J. R. Meteorol. Soc.* **2011**, *137*, 553–597. [CrossRef]
9. Kobayashi, S.; Ota, Y.; Harada, Y.; Ebita, A.; Moriya, M.; Onoda, H.; Onogi, K.; Kamahori, H.; Kobayashi, C.; Endo, H.; et al. The JRA-55 reanalysis: General specifications and basic characteristics. *J. Meteor. Soc. Jap.* **2015**, *93*, 5–48. [CrossRef]
10. Saha, S.; Moorthi, S.; Pan, H.-L.; Wu, X.; Wang, J.; Nadiga, S.; Tripp, P.; Kistler, R.; Woollen, J.; Behringer, D.; et al. The NCEP Climate Forecast System Reanalysis. *Bull. Amer. Meteor. Soc.* **2010**, *91*, 1015–1057. [CrossRef]
11. Silva, V.B.S.; Kousky, V.E.; Higgins, R.W. Daily precipitation statistics for South America: An intercomparison between NCEP reanalyses and observations. *J. Hydrometeor.* **2011**, *12*, 101–117. [CrossRef]
12. Huffman, G.J.; Adler, R.F.; Morrissey, M.M.; Bolvin, D.T.; Curtis, S.; Joyce, R.; McGavock, B.; Susskind, J. Global Precipitation at One-Degree Daily Resolution from Multisatellite Observations. *J. Hydrometeor.* **2001**, *2*, 36–50. [CrossRef]
13. Ploshay, J.J.; Lau, N.C. Simulation of the diurnal cycle in tropical rainfall and circulation during boreal summer with a high-resolution GCM. *Mon. Weather. Rev.* **2010**, *138*, 3434–3453. [CrossRef]
14. Medvigy, D.; Beaulieu, C. Trends in daily solar radiation and precipitation coefficients of variation since 1984. *J. Clim.* **2012**, *25*, 1330–1339. [CrossRef]
15. Deng, X.; Nie, S.; Deng, W.; Cao, W. Statistical evaluation of the performance of gridded monthly precipitation products from reanalysis data, satellite estimates, and merged analyses over China. *Theor. Appl. Climatol.* **2018**, *132*, 621–637. [CrossRef]
16. Akinsanola, A.A.; Ongoma, V.; Kooperman, G.J. Evaluation of CMIP6 models in simulating the statistics of extreme precipitation over Eastern Africa. *Atmos. Res.* **2021**, *254*, 105509. [CrossRef]
17. Sun, J.; Huang, Y.; Han, J.; Zhang, X. Comparison on Relationship between Western Pacific Subtropical High and Summer Precipitation over Dongting Lake Basin Based on Different Datasets. *Asia-Pacific J. Atmos. Sci.* **2021**, *57*, 663–678. [CrossRef]
18. Nie, S.P.; Wu, T.W.; Luo, Y.; Deng, X.; Shi, X.; Wang, Z.; Liu, X.; Huang, J. A strategy for merging objective estimates of global daily precipitation from gauge observations, satellite estimates, and numerical predictions. *Adv. Atmos. Sci.* **2016**, *33*, 889–904. [CrossRef]
19. Blacutt, L.A.; Herdies, D.L.; de Gonçalves, L.G.G.; Vila, D.A.; Andrade, M. Precipitation comparison for the CFSR, MERRA, TRMM3B42 and combined scheme datasets in Bolivia. *Atmos. Res.* **2015**, *163*, 117–131. [CrossRef]
20. Gehne, M.; Hamill, T.M.; Kiladis, G.N.; Trenberth, K.E. Comparison of global precipitation estimates across a range of temporal and spatial scales. *J. Clim.* **2016**, *29*, 7773–7795. [CrossRef]
21. Fu, G.; Charles, S.P.; Timbal, B.; Jovanovic, B.; Ouyang, F. Comparison of NCEP-NCAR and ERA-Interim over Australia. *Int. J. Climatol.* **2016**, *36*, 2345–2367. [CrossRef]
22. Huang, A.; Zhao, Y.; Zhou, Y.; Yang, B.; Zhang, L.; Dong, X.; Fang, D.; Wu, Y. Evaluation of multisatellite precipitation products by use of ground-based data over china. *J. Geophys. Res. Atmos.* **2016**, *121*, 10654–10675. [CrossRef]
23. Beck, H.E.; Vergopolan, N.; Pan, M.; Levizzani, V.; van Dijk, A.I.J.M.; Weedon, G.P.; Brocca, L.; Pappenberger, F.; Huffman, G.J.; Wood, E.F. Global-scale evaluation of 22 precipitation datasets using gauge observations and hydrological modeling. *Hydrol. Earth Syst. Sci.* **2017**, *21*, 6201–6217. [CrossRef]
24. Saha, S.; Nadiga, S.; Thiaw, C.; Wang, J.; Wang, W.; Zhang, Q.; Van den Dool, H.M.; Pan, H.-L.; Moorthi, S.; Behringer, D.; et al. The NCEP Climate Forecast System. *J. Clim.* **2006**, *19*, 3483–3517. [CrossRef]
25. Adler, R.F.; Huffman, G.J.; Chang, A.; Ferraro, R.; Xie, P.P.; Janowiak, J.; Rudolf, B.; Schneider, U.; Curtis, S.; Bolvin, D.; et al. The version-2 Global Precipitation Climatology Project (GPCP) monthly precipitation analysis (1979-present). *J. Hydrometeor.* **2003**, *4*, 1147–1167. [CrossRef]
26. Becker, A.; Finger, P.; Meyer-Christoffer, A.; Rudolf, B.; Schamm, K.; Schneider, U.; Ziese, M. A description of the global land-surface precipitation data products of the Global Precipitation Climatology Centre with sample applications including centennial (trend) analysis from 1901–present. *Earth Syst. Sci. Data* **2013**, *5*, 71–99. [CrossRef]
27. Bolvin, D. Global Precipitation at One-Degree Daily Resolution from Multisatellite Observations, Version 1.2. NASA GSFC, 2001. Available online: ftp://ftp.ncdc.noaa.gov/pub/data/gpcp/daily-v1.2/ (accessed on 1 September 2023).
28. Nie, S.P.; Luo, Y.; Li, W.P.; Wu, T.W.; Shi, X.L.; Wang, Z.Z. Quality control and analysis of global gauge-based daily precipitation dataset from 1980 to 2009. *Adv. Clim. Chang. Res.* **2012**, *3*, 45–53.

29. Nie, S.P.; Luo, Y.; Li, W.P.; Wu, T.W.; Shi, X.L.; Wang, Z.Z. A merging scheme for constructing daily precipitation analyses based on objective bias-correction and error estimation techniques. *J. Geophys. Res. Atmos.* **2015**, *120*, 8671–8692. [CrossRef]
30. Maggioni, V.; Meyers, P.C.; Robinson, M.D. A review of merged high resolution satellite precipitation product accuracy during the Tropical Rainfall Measuring Mission (TRMM)-era. *J. Hydrometeorol.* **2016**, *17*, 1101–1117. [CrossRef]
31. Xie, P.; Chen, M.; Shi, W. CPC global unified gauge-based analysis of daily precipitation. In Proceedings of the 24th Conference on Hydrology, Atlanta, GA, USA, 18–21 January 2010.
32. Cressman, G.P. An operational objective analysis scheme. *Mon. Weather. Rev.* **1959**, *87*, 367–374. [CrossRef]
33. Xie, P.P.; Chen, M.Y.; Yang, S.; Yatagai, A.; Hayasaka, T.; Fukushima, Y.; Liu, C. Agauge-based analysis of daily precipitation over East Asia. *J. Hydrometeor.* **2007**, *8*, 607–627. [CrossRef]
34. Wilks, D. *Statistical Methods in the Atmospheric Sciences*, 2nd ed.; Academic Press: Cambridge, MA, USA, 2006; p. 260.
35. Ebert, E.E.; Janowiak, J.E.; Kidd, C. Comparison of near-real-time precipitation estimates from satellite observations and numerical models. *Bull. Amer. Meteor. Soc.* **2007**, *88*, 47–64. [CrossRef]
36. AghaKouchak, A.; Mehran, A.; Norouzi, H.; Behrangi, A. Systematic and random error components in satellite precipitation data sets. *Geophys. Res. Lett.* **2012**, *39*, 9406. [CrossRef]
37. Nogueira, M. Inter-comparison of ERA-5, ERA-interim and GPCP rainfall over the last 40 years: Process-based analysis of systematic and random differences. *J. Hydrol.* **2020**, *583*, 124632. [CrossRef]
38. Saha, S.; Moorthi, S.; Wu, X.; Wang, J.; Nadiga, S.; Tripp, P.; Behringer, D.; Hou, Y.-T.; Chuang, H.-Y.; Iredell, M.; et al. The NCEP climate forecast system version 2. *J. Clim.* **2014**, *27*, 2185–2208. [CrossRef]
39. Trenberth, K.E.; Fasullo, J.T.; Mackaro, J. Atmospheric moisture transports from ocean to land and global energy flows in reanalyses. *J. Clim.* **2011**, *24*, 4907–4924. [CrossRef]
40. AghaKouchak, A.; Behrangi, A.; Sorooshian, S.; Hsu, K.; Amitai, E. Evaluation of satellite-retrieved extreme precipitation rates across the central United States. *J. Geophys. Res. Atmos.* **2011**, *116*, D2. [CrossRef]